water

MDPI

Article

Seasonal Three-Dimensional Hydrographic Variability of the Gulf of Thailand and Its Exchange with the South China Sea

Kittipong Phattananuruch [1], Tanuspong Pokavanich [2,*], Arachaporn Anutaliya [3], Anukul Buranapratheprat [4] and Xinyu Guo [5]

[1] Faculty of Fisheries, Kasetsart University, Bangkok 10900, Thailand; kittipong.pha@ku.th
[2] Department of Marine Science, Faculty of Fisheries, Kasetsart University, Bangkok 10900, Thailand
[3] Applied Physics Laboratory, University of Washington, Seattle, WA 98105-6698, USA; aanut@uw.edu
[4] Department of Aquatic Science, Faculty of Science, Burapha University, Chonburi 20131, Thailand; anukul@buu.ac.th
[5] Center for Marine Environmental Studies, Ehime University, Matsuyama 790-8577, Japan; guo.xinyu.mz@ehime-u.ac.jp
* Correspondence: ffistop@ku.ac.th; Tel.: +66-62-546-1999

Abstract

This study utilized a high-resolution, three-dimensional hydrodynamic model with improved model evaluation to investigate seasonal variations in key hydrographic conditions, including sea level, water temperature, salinity, current speed, and circulation in the Gulf of Thailand (GoT), as well as its interaction with the South China Sea (SCS). The analysis focuses on a climatological year calculated from a 15-year average for 2006–2020, which is categorized into four seasons: northeast monsoon, the first inter-monsoon, southwest monsoon, and the second inter-monsoon. Evaluation of model performance, based on observational data with temporal resolutions ranging from 30 min to monthly average with a duration from 10 months to 5 years, demonstrated good accuracy through high coefficients of determination and low root mean square errors. Results clearly depicted seasonal variability in hydrographic properties, characterized by alternating patterns of high and low sea level, high and low water temperatures, saline and fresh water, along with a persistent anticyclonic gyre in the central area of GoT and a smaller anticyclonic gyre in the southern area. Seasonal exchange flows between the SCS and the GoT were also evident, with the strongest outflow in northeast monsoon and the weakest in the second inter-monsoon.

Keywords: circulation; hydrodynamic; seasonal variability; simulation; volume transport

1. Introduction

The Gulf of Thailand (GoT) is a tropical sea located between latitude 6° N to 13.6° N and longitude 99° E to 105° E. The GoT is economically important for Southeast Asia countries serving fishery and aquaculture industries. In addition, the tourism and petroleum industry drives the economy of surrounding countries [1,2]. The GoT is bordered by the Indochinese Peninsula and connected to the South China Sea (SCS) through an opening in its southeastern boundary, classifying it as a semi-enclosed sea (Figure 1).

Received: 24 January 2026
Revised: 4 March 2026
Accepted: 18 March 2026
Published: 24 March 2026

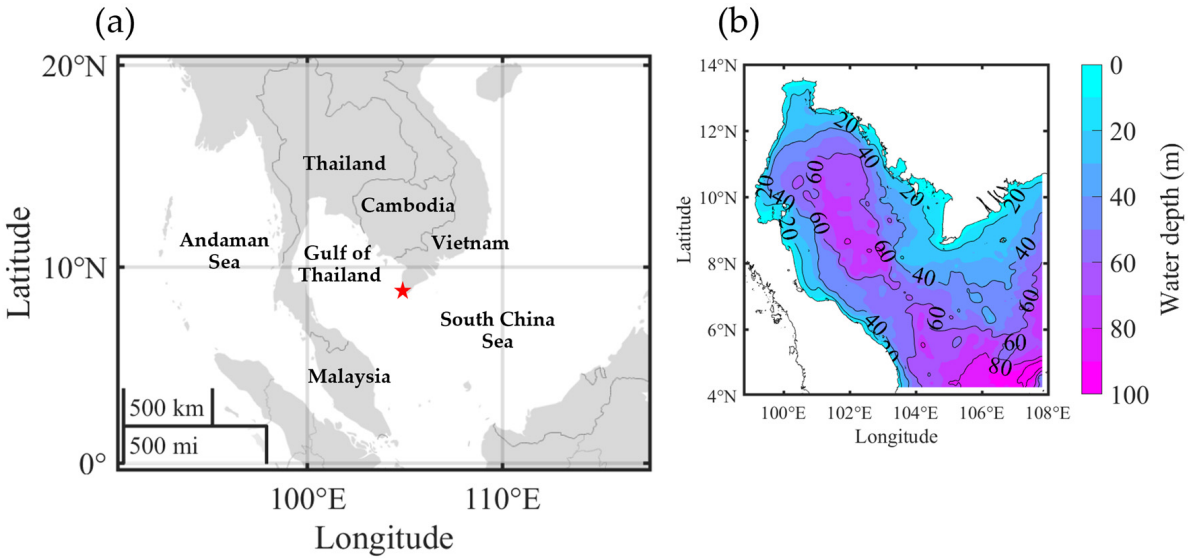

Figure 1. Overview of the Gulf of Thailand (GoT): (**a**) geographical position with a red star represents location of Ca Mau Cape (CMC); (**b**) bathymetry (m) with isolines showing depth intervals of 20 m.

Two monsoonal winds control seasons in this area, including the southwest monsoon (SWM) that prevails from mid-May to September, and the northeast monsoon (NEM) that dominates from November to February. The SWM brings moisture and humidity from the Indian Ocean to the Indochinese Peninsula, producing high rainfall and river discharge to the GoT and surrounding continents, and this season is known as the wet season. In contrast, during the dry season when NEM brings low temperature and dry air from high latitudes, air temperature over the GoT and the surrounding area drops and freshwater discharge is low, except the southern part of the peninsula, where rainfall is still high [3–5].

Previous observational and hydrodynamic modeling studies have demonstrated that, despite its relatively shallow depth, the GoT exhibits complex hydrographic features governed by multiple interacting processes. They include tidal forcing [6–9], monsoon winds [7–11], orographic effects [12], sea surface heat fluxes [5], freshwater inputs from rivers [5,9,13] and direct precipitation [14], as well as offshore boundary conditions associated with the adjacent SCS [5,9,15,16].

During the NEM, surface currents in the GoT tend to flow from east to west, driven by northeasterly winds. In addition, the intrusion of cold, dense water from the SCS into the GoT near the Ca Mau Cape (CMC)—a cape located in the southern part of Vietnam (red star in Figure 1a)—is detected. In contrast, during the SWM, surface currents move eastward, with a pronounced southeastward outflow from the GoT to the SCS [5,10]. A three-dimensional numerical model [8] revealed that clockwise and counterclockwise circulations developed in the GoT throughout the entire water column, with their positions shifting seasonally from the northern part of the GoT to the mouth of the gulf. In addition, opposite flow directions between the upper and lower layers were successfully simulated, with surface water outflow during the SWM and second inter-monsoon (INM2) coinciding with lower water inflow from the SCS [9,10,17].

Overall, the hydrographic conditions of the GoT are highly complex and driven by the combined effects of multiple forcing mechanisms. Numerous studies have shown that accurate simulation of ocean circulation critically depends on both the temporal and spatial variability of wind forcing. However, several earlier numerical studies of the GoT relied on monthly or seasonal mean datasets derived from relatively short and outdated periods or assumed spatially uniform wind fields. Such simplifications likely led to the omission of important wind-driven processes [8,10]. Moreover, investigations of water exchange be-

tween the GoT and the SCS remain limited. Although several studies have reported aspects of this exchange [3,5,9,18], subsurface transport processes are still poorly understood. For instance, Ekman transport through the GoT mouth has been estimated [4,15], and residence time within the GoT has been reported [9]. Nevertheless, some previous modeling studies applied simplified and unrealistic offshore boundary conditions due to data limitations at that time, which may have hindered realistic representation of GoT–SCS interactions. With the availability of modern forcing datasets and improved computational capabilities that allow finer spatial resolution, it is now possible to more accurately capture and characterize hydrodynamic conditions [19,20].

In this study, we employ a three-dimensional hydrodynamic model, rigorously evaluated model performance against extensive observational data. The details of the model's evaluation will be presented in Section 3.1. The model incorporates temporally and spatially varying tides, monsoonal winds, surface heat fluxes, freshwater inputs from rivers, evaporation and precipitation over the sea, and depth-dependent offshore temperature, salinity, and subtidal currents. The combined influence of these forcings produces strongly spatial and temporal variations in three-dimensional hydrodynamics and enhances connectivity between the GoT and the SCS, which have not been adequately represented in previous studies.

2. Materials and Methods

2.1. Hydrographic Field Data

We used hourly tidal data (2016–2020) from five tidal stations—Laem Sing, Hua Hin, Ko Lak, Ko Mattaphon, and Ko Prap (Figure 2)—to evaluate the model's accuracy; these datasets were provided by the Hydrographic Department, Royal Thai Navy. Hourly water level data for the same period, measured at the Vung Tau station in Vietnam, were used to evaluate model performance outside the GoT area. These data are provided by the University of Hawaii Sea Level Center, https://uhslc.soest.hawaii.edu/ (accessed on 22 January 2024). Monthly mean sea level data from the Geting station in Malaysia, https://psmsl.org/data (accessed on 22 January 2024) were also utilized to evaluate model performance.

We deployed the HOBO® U20L Water Level Logger (U20L-01) and HOBO® U24 Conductivity Logger (U24-002-C), HOBO®, Bourne, MA, USA, to collect water level, water temperature, and conductivity data at 30 min intervals from 2018 to 2019 at Sriracha, Chonburi province in the Upper Gulf of Thailand (UGoT). The same measurement protocol was applied at Ko Mannai (Mannai Island), Rayong Province, Thailand (October 2019), and Ko Tao (Tao Island), Surat Thani Province, Thailand (March 2020). Details of the data logger deployment are provided in Table A1. Simultaneously, in 2020, the Hydro-Informatics Institute (HII) established the marine real-time measurement system at Sriracha (Station GOT001), providing continuous measurements of water level, water temperature, salinity, and current velocity. These datasets were used to verify model effectiveness.

Additionally, water temperature and salinity profile data collected by M.V. SEAFDEC 2 (17 August–19 September 2018) and provided by the Southeast Asian Fisheries Development Center (SEAFDEC) were used to evaluate the simulated spatial distributions. Monthly mean sea surface velocity from SEAWATCH buoys [21] and trajectories of current near-surface satellite-tracked drifters, obtained from the marine observation and modeling database system for oceanography research in Thailand, https://hydro-hims.hii.or.th/ocean/buoy.php (accessed on 29 December 2025), were compared against the modeled seasonal mean circulation.

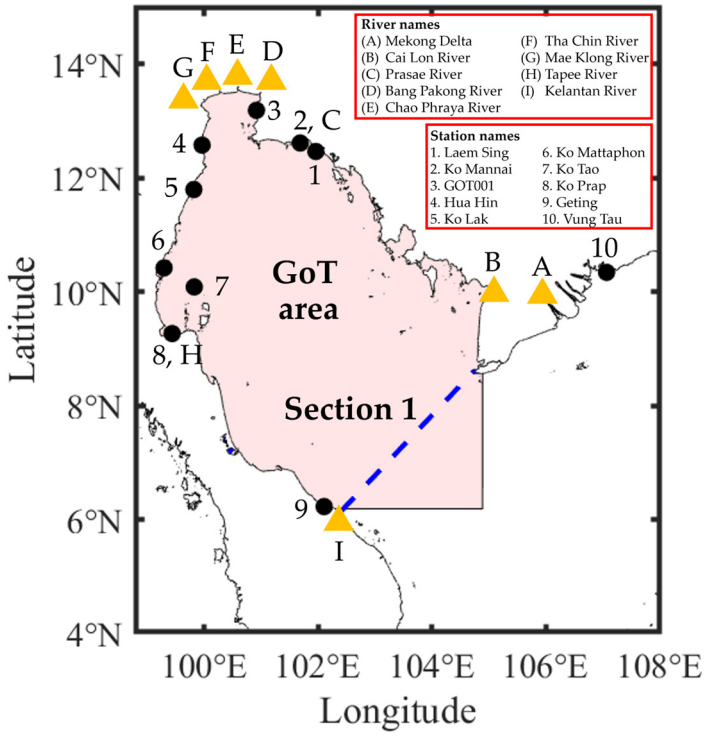

Figure 2. Locations of measurement stations, rivers, analysis area (light red shading), and a section line (a blue dashed line).

2.2. Hydrodynamic Modeling

Hydrodynamic variations in the GoT were simulated using two approaches: a Climatological Model (Model C) and an Evaluation Model (Model E), both implemented with Delft3D-FLOW program version 4.04.01 [22]. Delft3D-FLOW solves the unsteady hydrodynamic equations and simulates non-steady flow and the transport of water and particles in both freshwater and marine environments. The program incorporates tidal forcing and meteorological inputs and supports both 2D and 3D hydrodynamic and transport simulations. Further technical details are described by [22].

Model E was configured for the period 2015–2020 to evaluate the model's performance. Thereafter, Model C was configured to represent the general hydrodynamic characteristics of the GoT, including water temperature, salinity, density (sigma-t), and circulation. Both models utilized rectangular grids of 349 × 376 for the computational domain covering the entire GoT. Each grid has a horizontal resolution of 0.025° × 0.025°, which is approximately 2.8 km on each side. The models included 10 vertical layers (σ coordinates). The analysis area and a section line shown in Figure 2 were used to present the hydrographic distribution of the GoT.

Bathymetric data were collected from two sources: nearshore data were obtained from Thai nautical charts, and offshore data were retrieved from the General Bathymetric Chart of the Oceans (GEBCO), using the GEBCO_2020 grid dataset, https://download.gebco.net/ (accessed on 21 September 2020). The used nautical charts included chart number 001, 102, 112, 114, 117, 137, 141, 164, 203, 204, 205, 206, 224, 228, 227, and 248 published by the Hydrographic Department, Royal Thai Navy. Shoreline data were downloaded from GSHHG dataset, version 2.3.7, available at https://www.soest.hawaii.edu/pwessel/gshhg/ (accessed on 19 December 2020).

The simulation was initialized under calm sea conditions, with zero sea level changes and zero current speed. Water temperature and salinity fields were interpolated from the Global Ocean Forecasting System (GOFS) 3.1: 41-layer HYCOM + NCODA Global 1/12°

Analysis dataset, https://www.hycom.org/dataserver/gofs-3pt1/analysis (accessed on 29 March 2024). This dataset provides global oceanographic fields across 40 vertical layers, ranging from the surface (0 m) to a depth of 5000 m. Model E was initialized using water temperature and salinity data from 1 January 2015, while Model C was initialized with the 15-year climatological mean from 1 January spanning 2006–2020.

The hydrodynamic model was forced by sea level variations at the open boundaries, using fourteen tidal constituents from the TPXO9-atlas (v4) [23], extracted with the Tide Model Driver (TMD) version 2.5 [24]. To incorporate the sea level cycle of the SCS [6,25] into the model, a sinusoidal signal with a 20 cm amplitude, 365.02-day period, and 278.1° phase was added. Furthermore, boundary conditions for depth, varying water temperature, and salinity were retrieved from the GOFS at 3 h intervals.

Spatial meteorological forcing data with 3 h intervals, including mean sea level pressure, wind speed and direction at 10 m height above surface, total precipitation, total cloud cover, and relative humidity, were obtained from the ERA5 global reanalysis dataset by the European Center for Medium-range Weather Forecasts (ECMWF), available at https://cds.climate.copernicus.eu/datasets, (accessed on 19 October 2024). The ERA5 provides global atmospheric, land surface, and ocean wave parameters at hourly resolution and spatial resolution ranging from 0.25° to 1°. Further details are described by [26].

Freshwater inputs in the model included precipitation, and river discharge from principal rivers surrounding the GoT, which are the Mekong Delta, Cai Lon River, Prasae River, Bang Pakong River, Chao Phraya River, Tha Chin River, Mae Klong River, Tapee River, and Kelantan River. We utilized daily river discharge data from the Global Flood Awareness System (River discharge and related historical data; https://ewds.climate.copernicus.eu/datasets/cems-glofas-historical?tab=overview (accessed on 30 April 2021)). This dataset covers global freshwater variable (excluding Antarctica); it has a horizontal resolution of 0.05° × 0.05° and covers the period from January 1979 to present. Further details are provided by [27].

For Model C, all forcing data and inputs were averaged over the period 2006–2020 to produce climatological forcing data. These datasets were then applied to the model at initial state and ran for 2 years, allowing the spin-up of the model; the spin-up time is based on the estimated flushing time of water in the GoT [9]. The results from the third simulation year were selected for analysis. On the other hand, for Model E, which used initial conditions interpolated from the GOFS, we applied only a 1-year spin-up period, with the simulation starting in 2015. Detailed model specifications are provided in Table A2.

2.3. Model Evaluation

Performance of the Model E was evaluated using the coefficient of determination (R^2) (Equation (1)) and the root mean square error (RMSE) (Equation (2)). Due to variations in the measurement periods of the hydrographic field data, model outputs were compared against observational data across multiple temporal resolutions, ranging from 30 min intervals to the monthly mean. The current velocity measured for the GOT001 station was filtered to eliminate fluctuation with a period longer than 3 h. The specific evaluation periods used in the comparison are summarized in Table A3.

$$R^2 = \frac{\left(\sum_{i=1}^{N}\left(C_{ai}-\overline{C_a}\right)\cdot\left(C_{si}-\overline{C_s}\right)\right)^2}{\sum_{i=1}^{N}\left(C_{ai}-\overline{C_a}\right)^2\cdot\sum_{i=1}^{N}\left(C_{si}-\overline{C_s}\right)^2} \quad (1)$$

$$RMSE = \sqrt{\frac{\sum_{i=1}^{N}(X_i-Y_i)^2}{N}} \quad (2)$$

where C_{ai} represents the observed data at time step i, $\overline{C_a}$ denotes the average of observed data C_{ai}, C_{si} is the model results at time step i, $\overline{C_s}$ is the average of model results, X_i is the observed data at time step i, Y_i is the model results at time step i, and N is the total number of data used in the analysis.

2.4. Data Analysis

Model outputs for entire GoT were averaged to monthly means to investigate seasonal variations in the key hydrographic variables, including water level, water temperature, salinity, density (sigma-t), and circulation. The seasonal classification was defined as follows: January, February, and December for the NEM, March to May for the first inter-monsoon (INM1), June to August for the SWM, and September to November for the INM2.

We examined the horizontal distribution of hydrographic variables at three depths (1 m, 30 m, and 50 m) to represent the near-surface, middle, and bottom layers, respectively, within a climatological year. Seasonal current components normal to Section 1 (Figure 2) are used to characterize the GoT–SCS water exchange, with the volume transport across the GoT boundary to quantify its seasonal variability.

3. Results and Discussion

3.1. Performance of the Model

The model generally reproduces variations in water level, water temperature, salinity, and flow velocity, as evaluated by the R^2 and RMSE values at each station (Table 1). These evaluations cover short-term variations (hourly intervals), seasonal variations to interannual variations, depending on the periods of available data. All stations exhibit satisfactory water level changes with high R^2 values, and much smaller RMSE than the tidal range (0.5 m to 4 m). The monthly mean water level at Geting station during 2016–2017 displays reasonable agreement between the simulated and observed data, with higher values at the beginning and end of the year, and lower values during the middle of the year (Figure 3a). It is noted that the simulated water levels are slightly lower than the measured values.

Table 1. Performance of Model E, presented in terms of RMSE and R^2 values.

Stations	Variables	RMSE	R^2
Laem Sing	Water level	0.17 m	0.88 *
Ko Mannai	Water temperature	0.87 °C	0.83 *
Sriracha (GOT001)	Water level	0.30 m	0.88 *
	Water temperature	0.91 °C	0.70 *
	Salinity	1.78	0.48 *
	Eastward velocity (3 h filtered)	0.03 m s^{-1}	0.22 *
	Northward velocity (3 h filtered)	0.05 m s^{-1}	0.80 *
	Total magnitude (3 h filtered)	0.05 m s^{-1}	0.42 *
Hua Hin	Water level	0.22 m	0.90 *
Ko Lak	Water level	0.13 m	0.92 *
Ko Mattaphon	Water level	0.14 m	0.91 *
Ko Tao	Water level	0.16 m	0.88 *
	Water temperature	0.97 °C	0.81 *
Ko Prap	Water level	0.19 m	0.87 *
Geting	Water level	0.08 m	0.91 *
Vung Tau	Water level	0.17 m	0.96 *

Note: * R^2 is statistically significant at a 95% confidence level.

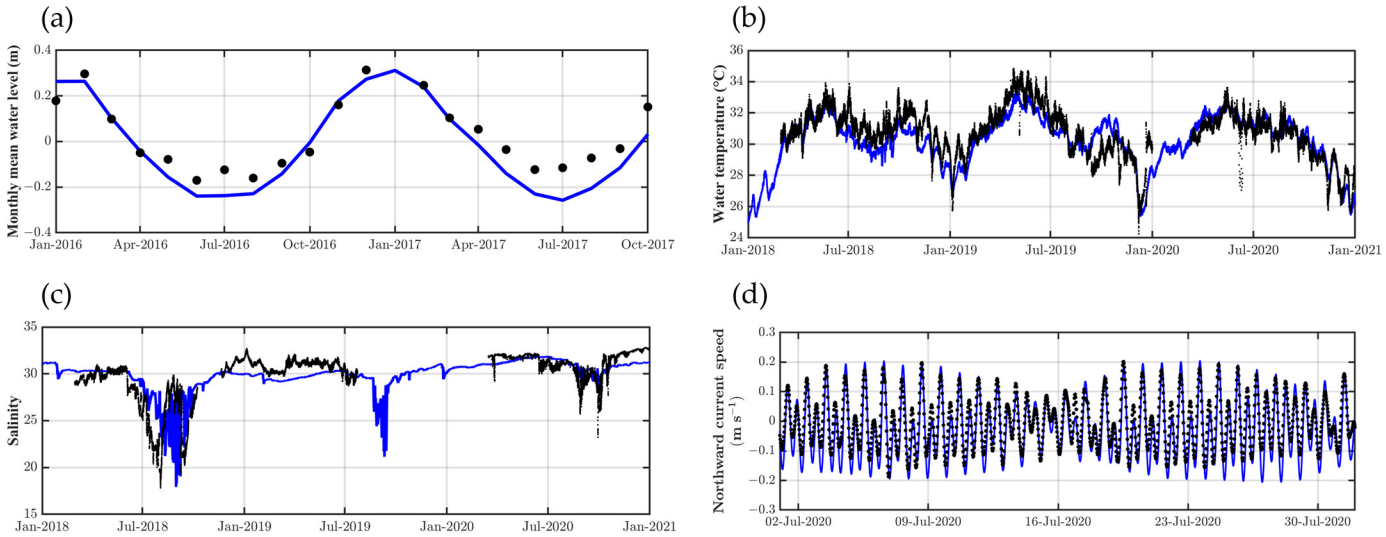

Figure 3. Evaluation of Model E, where black dots represent measurement data and blue lines represent the model results: (**a**) monthly mean water level at the Geting station; (**b**) water temperature at station GOT001; (**c**) salinity at station GOT001; (**d**) 3 h filtered northward current speed at station GOT001.

Water temperatures at Ko Mannai, GOT001, and Ko Tao stations are comparable to the observed data, with RMSE values less than 1 °C. In particular, the results at GOT001 station capture both seasonal and interannual variations effectively (Figure 3b). However, the simulated water temperatures are generally underestimated. We hypothesize that the discrepancy may be attributed to the deployment method of the temperature loggers. Specifically, the loggers were installed inside a polyvinyl chloride (PVC) pipe with perforations intended to allow for a water flow. We suspect that the number and size of these perforations were insufficient, leading to restricted water circulation and trapped heat retention within the pipe, which could have resulted in unrealistically elevated temperature. Notably, the model exhibited less underestimation in 2020 at station GOT001, coinciding with a revision of deployment approach that did not enclose the logger in a pipe. The simulated salinity at GOT001 also represents both seasonal and interannual variations (Figure 3c), although they do not perfectly align with the observed data. This discrepancy may be ascribed to the model's insufficient resolution of freshwater, which is too coarse to accurately represent the abrupt change in the local input of freshwater at the GOT001 location.

The model demonstrates greater accuracy in simulating the northward (meridional) current velocity component compared to the eastward (zonal) component, as reflected by a significantly higher R^2 value, despite a slightly larger RMSE. The lower accuracy in simulating the eastward component of current may result from local bathymetry and sub-grid scale turbulences caused by dense green mussel aquaculture rafts that influence current velocity [28] near station GOT001. Additionally, the eastward current is a minor flow component in this area (current speed less than 0.1 m s^{-1}), unlike the northward component (current speed greater than 0.1 m s^{-1}). As a result, the northward velocity is less affected by the aquaculture structure and displays a stronger agreement with the model simulations (Figure 3d). In addition, the model's accuracy for total magnitude is poor (R^2 = 0.42), with results being overestimated. These differences confirm the effect of the aquaculture rafts, which can reduce measured current magnitude (both northward and eastward current velocities). Comparisons with monthly sea surface flow velocity from the SEAWATCH buoys and trajectories of the satellite drifters display good agreement with different stations around the GoT (Figures A1 and A2).

The model shows an overall fair reproduction of the horizontal distributions of water temperature and salinity when compared with measurements collected by M.V. SEAFDEC 2 (Figure 4). At the 10 m depth, the simulated water temperature generally reproduces the observed spatial patterns (Figure 4a); however, the model tends to underestimate temperatures, particularly in the northern part of the GoT (11–13° N). At the 40 m depth, the simulation does not fully capture the observed temperature distribution, with underestimation in the central region (9–10° N) and overestimation in the western and southern gulf. The simulated salinity fields exhibit comparable spatial distributions at both 10 m and 40 m depths (Figure 4b), successfully capturing the low-salinity conditions in the UGoT and the higher salinity values in the western and southern regions.

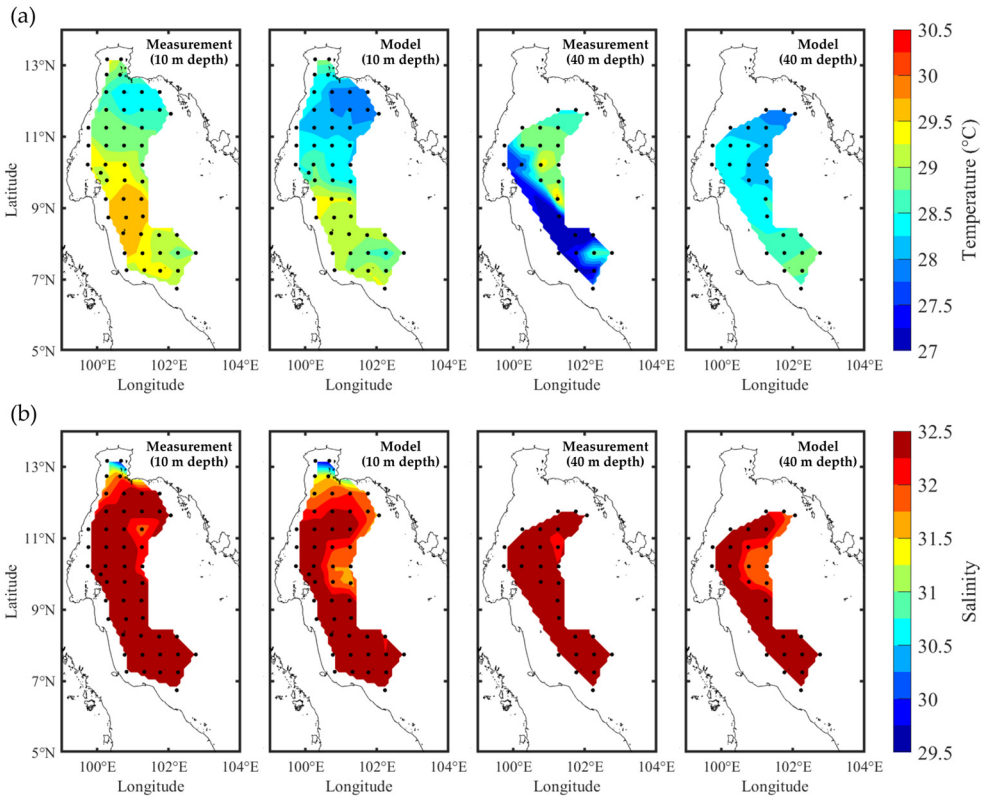

Figure 4. Comparison of measured and simulated spatial distributions at depths of 10 m and 40 m: (**a**) water temperature; (**b**) salinity. Black dots represent observation stations of M.V. SEAFDEC 2 (17 August–19 September 2018).

These discrepancies may be attributed to the atmospheric forcing data, whose 0.25° spatial resolution may be too coarse to resolve small-scale variability in winds, surface heat, and freshwater fluxes that strongly influence temperature and salinity structures. These variations may be accounted for by biases in ERA5 forcing, consistent with the findings of [20] regarding the Adriatic Sea. However, further analysis is required to confirm the observed biases within the GoT. In addition, uncertainties in the offshore boundary conditions derived from the GOFS may contribute to the mismatch, as the model may not adequately represent intermittent intrusions of relatively cooler and higher-salinity bottom water from the SCS into the GoT. Nevertheless, the model successfully captures the seasonal variability of the Gulf's hydrographic properties.

3.2. Seasonal Characteristics of the GoT's Hydrography

3.2.1. Water Level Variations

The average water level in the GoT exhibits clear seasonal variations (Figure 5). The highest levels are observed during the NEM (0.3 m above mean sea level), followed by a decline during the INM1, reaching a minimum during the SWM (0.3 m below mean sea level), and gradually rising again during the INM2. Spatial differences in water levels are also evident across seasons. Notably, lower water levels are observed in the UGoT and upper part during the NEM. In contrast, during the other seasons, mounds of higher water levels tend to occur in the central part of the GoT (approximately 9–11° N). Additionally, slight variations are observed in the southwestern part of the GoT (around 7–8° N, 102° E). The distinct seasonal variations in water levels during the NEM and the SWM are consistent with remote sensing data. These data indicate that water levels in the GoT are significantly higher or lower compared to those in the SCS, primarily driven by monsoonal wind patterns [11,29,30].

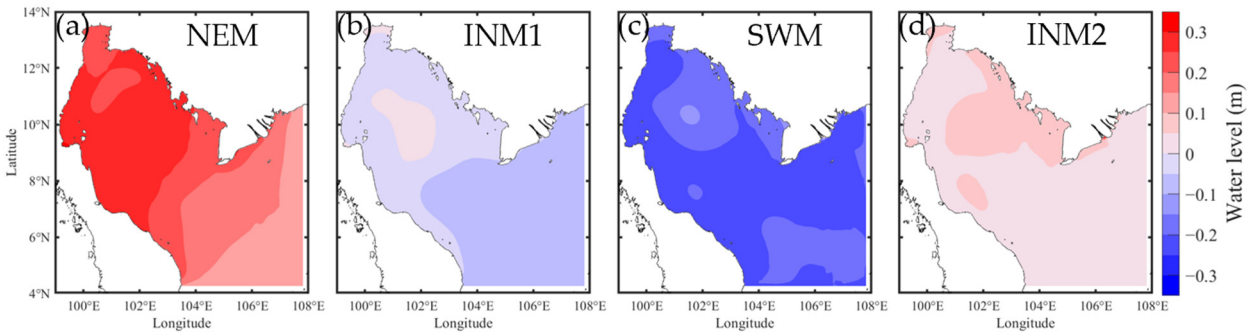

Figure 5. Seasonal distribution of water level during: (**a**) the northeast monsoon (NEM); (**b**) the first inter-monsoon (INM1); (**c**) the southwest monsoon (SWM); (**d**) the second inter-monsoon (INM2).

3.2.2. Water Temperature Variations

At the surface (1 m depth), water temperature is consistently warmer in nearshore areas than in offshore areas across all seasons. This pattern is particularly evident along the eastern GoT, including the coastal zones of Thailand, Cambodia, and Vietnam, as well as in the southern GoT near southern Thailand and Malaysia (Figure 6a–d). Water temperature in the GoT is the lowest during the NEM (~28 °C) and the highest during the INM1 (~30 °C), with temperatures generally higher inside the GoT as compared to the SCS.

Warmer water temperature appears in the eastern part of the GoT during the NEM, with a further noticeable increase in the INM1 (Figure 6a,b). The occurrence of warm water is likely due to reduced latent heat, resulting from weakened winds caused by the orographic blocking effect of the Cardamom Mountains located on the adjacent continental landmass [12]. Additionally, in the southern part of the GoT near the mouth (approximately 6° N, 102° E), water temperature was the highest locally during the SWM.

At 30 m depth (Figure 6e–h), temperatures are lower than at the surface and exhibit a distinct spatial pattern compared to the surface layer. The highest temperature at this depth occurs in the INM2 (~28.5 °C), while the lowest one occurs in the NEM (~28 °C). During the NEM, cool water (27 °C) from the SCS begins to enter the GoT and gradually fills the basin at this depth and below in the following seasons. Water pools with the temperature approximately 0.5 °C higher than the surrounding waters are found in the INM1 and the SWM at center of the GoT. Variations in water temperature at the 50 m depth (Figure 6i–l) show slight differences compared to shallower depths, with the highest values in the INM2 (~28 °C) and the lowest in the INM1 (~27.4 °C). A full intrusion of the SCS cold water caused the temperature to decrease from the NEM to the INM1, while warmer water still

appeared in the SWM at the center of the GoT, coinciding with low temperatures (27 °C) observed in the deepest area of the GoT.

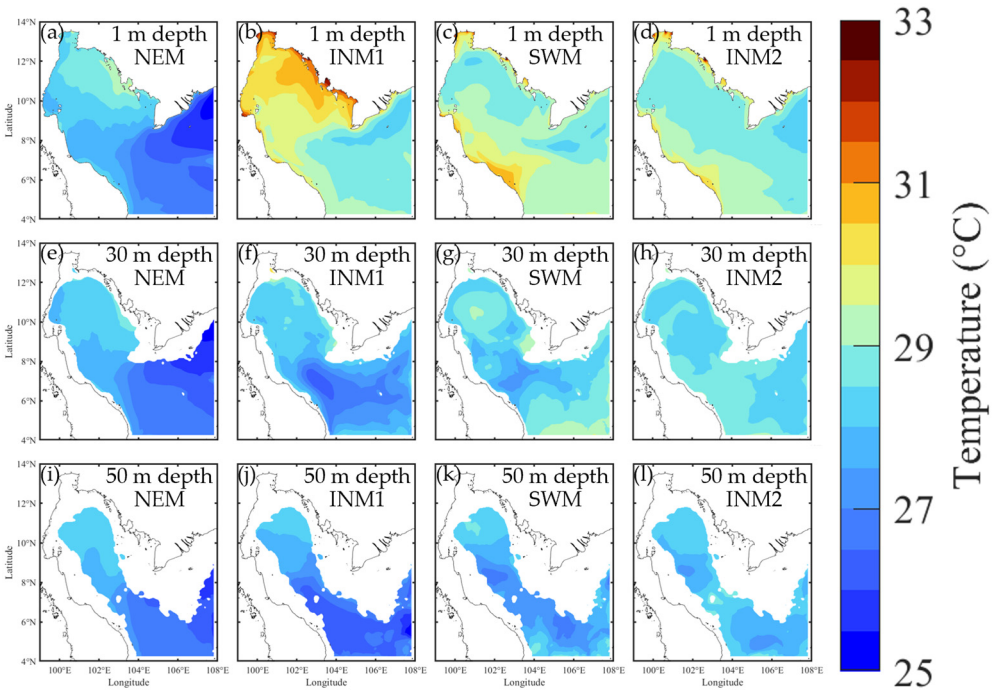

Figure 6. Seasonal distributions of water temperature in the GoT at: (**a**–**d**) 1 m; (**e**–**h**) 30 m; (**i**–**l**) 50 m depth.

A winter cold tongue, characterized by SST below 26 °C in the southwestern of the SCS, near the southern region of the CMC, is found during the NEM, consistent with previous studies (e.g., [31,32]). However, our results show some differences in the spatial extent of the cold tongue. Specifically, the cold tongue in our study covers a smaller area than that reported by [31] and exhibits broader spreading in February, in contrast to the report of [32], where the widest extent was presented in late January. These may result from differences in the study periods; for instance, ref. [32] analyzed the data from 1982 to 2012, while our study focuses on the period from 2006 to 2020, suggesting the interannual variability in the SST. The difference may reflect a long-term variation in the GoT-SCS interaction. Our simulated surface temperature aligns more closely with the climatological seasonal surface temperature (averaged over 16 years from 2003 to 2018) reported by [17], as compared to the results of [10]. These discrepancies may be attributed to the use of higher-resolution forcing data and a finer computational grid, which provide improved results in our study [19,20].

3.2.3. Salinity Variations

Surface salinity at the 1 m depth peaks during the INM1 (Figure 7b) and reaches its minimum during the INM2 (Figure 7d), with slightly higher values in the NEM (Figure 7a). Although precipitation is greater in the INM1 than in the NEM, salinity remains elevated, indicating intrusion of high salinity water from the SCS. In contrast, low salinity water appears near river mouths and along the coast during the NEM but is largely absent in the INM1. The disappearance of the low salinity plume in the UGoT from the INM2 to the NEM suggests a flushing time of 3 months, consistent with residence time estimates for this area [9]. A salinity pool is present in the central GoT throughout the year, although its values and location vary slightly among seasons.

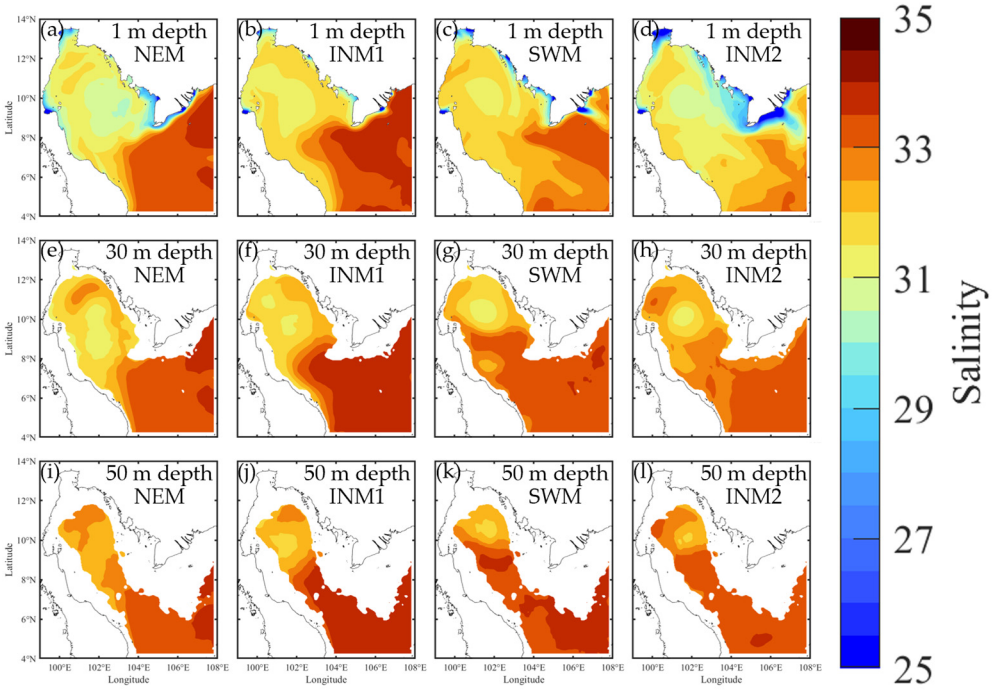

Figure 7. Seasonal distributions of salinity in the GoT at: (**a**–**d**) 1 m; (**e**–**h**) 30 m; (**i**–**l**) 50 m depth.

During the NEM, two distinct salinity pools, one higher than 31 and another less than 31, are found. The low-salinity pool shifts slightly eastward in the INM2. The locations of these low salinity pools correspond to patterns in water level, where elevated water levels correspond to reduced salinity. A similar low-salinity pool in November was also reported [3]. However, its characteristics were not comprehensively described, presumably due to a lack of sufficient observational data. During the NEM, the water observed in the western GoT (7–11° N) exhibits the lowest salinity compared to other seasons. This low-salinity water likely originated during INM2 in the UGoT and was gradually transported to the western GoT [16]. This movement of low-salinity water may explain the observed low-salinity water extending from 8° N to 11° N during the NEM, as reported by [10].

At 30 m depth, salinity is the highest during the SWM (Figure 7g) and the lowest during the NEM (Figure 7e), with values generally exceeding those at 1 m depth. Seasonal salinity variation at this depth remains below 0.6. At the 50 m depth, highest salinity values are observed during the SWM (Figure 7k) with less seasonal variation (~0.4). High-salinity water (>33) from the SCS begins to enter the GoT during the NEM (Figure 7i) and continues through the SWM, potentially reaching as far north as 9° N during the SWM before declining in INM2 (Figure 7l). The salinity pools may result from upwelling and downwelling processes driven by water divergence and convergence, as reported in previous studies [3,16,33]. Ref. [17] reported that the mixing induced by clockwise and counterclockwise circulations in the central GoT can reduce the penetration of the more saline water from the SCS. As a result, water with salinity levels below 31 has been observed at greater depths.

Salinity is consistently lower in the GoT than in the SCS throughout all seasons. Low salinity in the GoT is primarily attributed to freshwater input (river discharge and direct precipitation) and salty water from the SCS, further influenced by wind- and tide-driven mixing. The effect is particularly pronounced during the SWM and the INM2, when the winds prolong the presence of low-salinity conditions [3,5,9]. Although the SCS receives substantial freshwater input from the Mekong River, the resulting dilution remains confined to its coastal zone. This freshwater is then transported toward the GoT by wind-driven currents [16], contributing to salinity variation in the GoT [4]. High-salinity water (33)

begins to enter the GoT during NEM and fully penetrates through its mouth during INM1, especially along the Vietnam coast. In contrast, during INM1, low-salinity water outflow is found in the southwestern region, and by INM2, it expands to cover most of the mouth area. This pattern is consistent with both observational data and the other simulations (e.g., [10,17,34]).

3.2.4. Water Density Variations

Seasonal variations in water density are reflected in the horizontal distribution of sigma-t (σ_t; water density referenced to 1000 kg m^{-3}; Figure 8), which exhibits a pattern similar to salinity. However, the highest water density at depth of 1 m occurs during the NEM (Figure 8a), primarily due to lower water temperatures, especially the water outside the GoT, whereas the lowest density is observed during the INM2 (Figure 8d). In contrast, salinity reaches its maximum during the INM1 (Figure 7b).

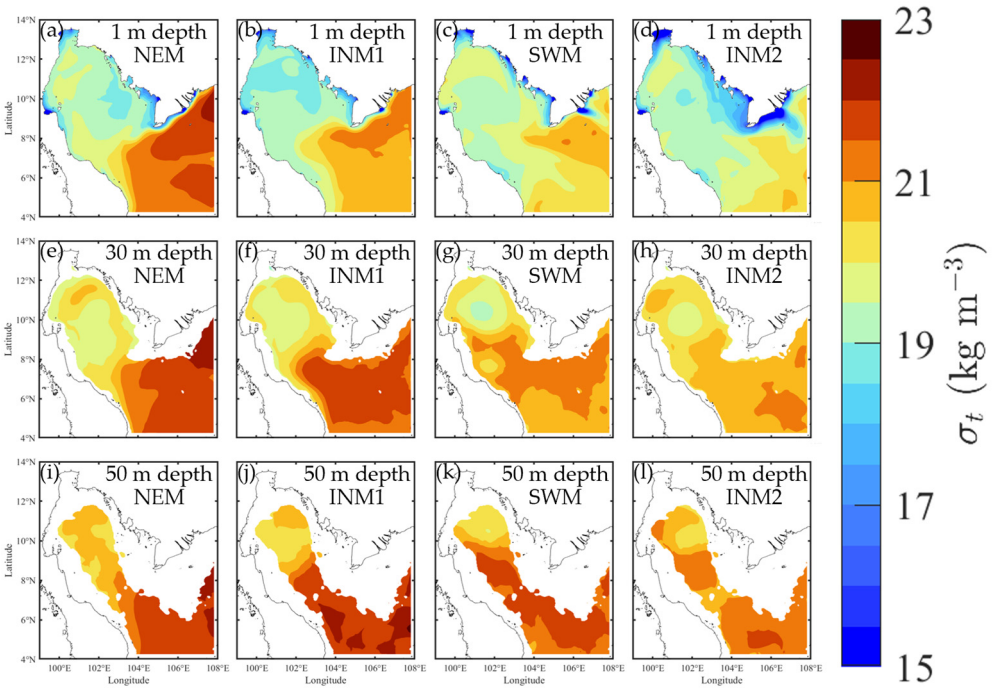

Figure 8. Seasonal distributions of water density in the GoT at: (**a**–**d**) 1 m; (**e**–**h**) 30 m; (**i**–**l**) 50 m depth.

Across all seasons, sigma-t values are consistently lower inside the GoT than outside, with values typically below 20 kg m^{-3}. The greatest (smallest) contrast of sigma-t between inside and outside appears during the NEM (INM2) when the spreading out of low density water from the GoT to the south at the surface layer highlights the influence of salinity contribution to density distribution. Surface water intrusion is evident during the NEM and INM1 (Figure 8a,b), particularly in the southern region near CMC. In contrast, low-density water begins to flow outward from the southern GoT during the SWM (Figure 8c) and becomes more widespread in the INM2 (Figure 8d). Low sigma-t zones are notably present during the SWM and INM2.

At the 30 m depth, sigma-t values are the lowest in the NEM (Figure 8e) and display increases from the SCS through the GoT, starting from this season until filling over the GoT in the SWM (Figure 8g), when the sigma-t values reach their maximum. Water density at this depth is higher than at 1 m depth and displays less spatial variability, with a distinct low-density pool forming in the central to lower GoT region, which is consistent with the observation reported by [3,34]. During the NEM, higher-density water from the SCS

(sigma-t > 20 kg m^{-3}) begins to enter the GoT, reaching the central basin during the SWM before retreating in the INM2 (Figure 8h).

The distribution of water density at the 50 m depth confirms the intrusion of the SCS water starting from the NEM to SWM (Figure 8i–k) and clearly displays estuarine circulation of the GoT, with denser water from the SCS entering further to the center of the GoT to compensate for the outflow of freshwater at the surface during the SWM. Furthermore, lower density water compared to surround water is observed at the central part coinciding with the upper depth.

Our results are comparable with the NAGA cruise [3], especially in the INM1 and SWM, and the study of [34] during the INM1. Greater discrepancies are observed in other seasons, potentially due to differences in the investigation periods (i.e., specific years versus climatological averages). These discrepancies are likely driven by temporal variations in freshwater input and surface heat fluxes.

3.2.5. Current and Circulation Variations

The speed and direction of circulation in the GoT exhibit obvious seasonal variations. A clockwise circulation pattern is consistently found at the central GoT (8–12° N) across all seasons and depths (Figure 9), with particularly strong intensity and well-defined gyre during the SWM (Figure 9g–i) and the INM2 (Figure 9j–l).

In general, currents at a depth of 1 m are stronger than those at 30 m and 50 m and may occasionally flow in different directions. The current speed in the UGoT is consistently lower than the average current speed found throughout the GoT. During the NEM, strong southwestward flow at 1 m depth from the SCS bifurcate at the eastern coast of southern Thailand at ~6° N, forming a strong northward (southward) flow to its north (south). The northward branch serves as the western flank of a clockwise circulation centered at 10° N, 102° E (Figure 9a). Additionally, a smaller counterclockwise circulation occasionally develops north of the primary clockwise gyre, with its western flank being the southward flow originating from the UGoT. In the INM1, a strong northward and southward flow along the western coast of the GoT is still evident (Figure 9d). Also, the westward currents from the SCS are present, while shifted slightly northward merging with the clockwise circulation centered at 9° N, 102° E. The inflows from the south subsequently exit the GoT along the southern coastline.

During SWM, current speeds increase significantly, exhibiting two notable clockwise circulations located in the central and southern regions of the GoT that persist at both the 1 m and the 30 m depth (Figure 9g,h). Additionally, a strong outward flow from the GoT is observed. During the INM2 period, the general current speed in the GoT generally decreased, while the two previously identified clockwise circulations remain evident at both depths (Figure 9j,k). In this period, a pronounced southward flow due to the freshwater discharge from the UGoT appears at western coast of the GoT (10–11° N). A clear inflow from the SCS is observed at the CMC, contributing to the development of another counterclockwise circulation pattern.

Opposite current directions are evident at the 30 m depth during the NEM (Figure 9b) and the SWM (Figure 9h), with southward and northward flows opposing the surface currents, respectively. In contrast, circulation during the INM1 (Figure 9e) and INM2 (Figure 9k) resembles the 1 m depth pattern, particularly the clockwise circulation. At the 50 m depth (Figure 9c,f,i,l), the circulation pattern is similar to that at 30 m, but with noticeably weaker current speeds. A stronger inward flow from the SCS in the INM1 to SWM periods indicates an increased intrusion, which corresponds with other water properties such as lower temperature, higher salinity, and increased sigma-t. These results are consistent with previous observation [3,34] and hydrodynamic model results [8,17].

It is important to note that although both our study and previous works [9,17] utilized climatological data to reproduce hydrographical fields in the GoT, some discrepancies remain. These differences may result from variations in model configurations, such as computational grid resolution—an important factor highlighted by [8,19]. Our study employed a finer grid resolution compared to earlier models, which may allow presence of more detailed structure in the simulation of physical processes.

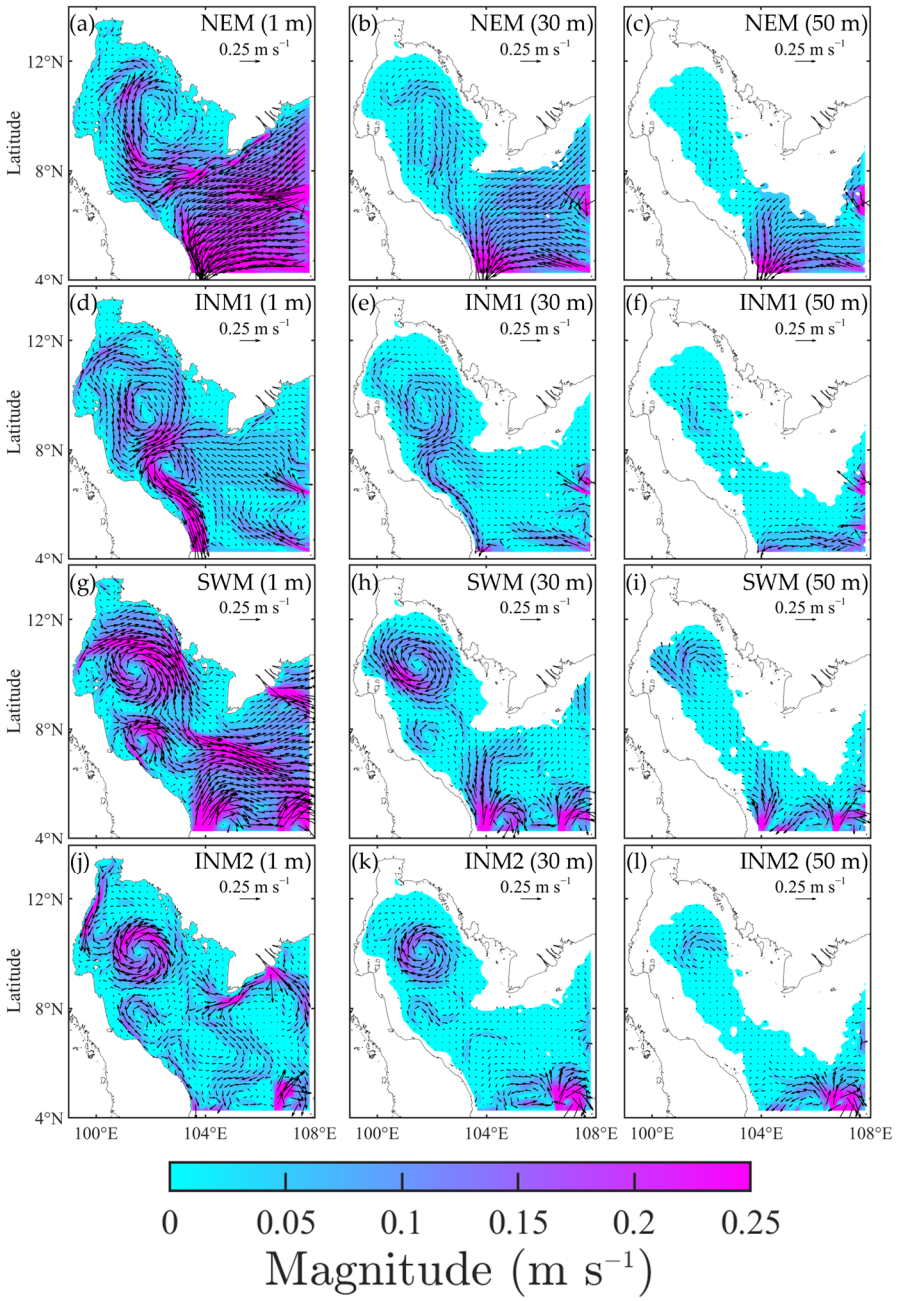

Figure 9. Monthly mean circulations patterns at 1 m, 30 m, and 50 m depths during the four seasons: (**a**–**c**) NEM; (**d**–**f**) INM1; (**g**–**i**) SWM; (**j**–**l**) INM2.

Our results reveal a persistent clockwise circulation in the central GoT year-round, whereas the NAGA expedition reported a counterclockwise pattern with a high salinity pool in November [3]. This feature also appears in our model but with reduced extent and salinity. The simulated circulation agrees well with previous studies during the NEM [11,29,31], but displays weaker agreement in other seasons, likely due to temporal wind variability, residual tidal signals, and differing seasonal definitions and forcing

datasets [8,16,29]. Although the model does not correspond well with the observed north–south flows in the western GoT [16], the overall circulation does so, particularly the clockwise circulation pattern in the central basin. Remaining discrepancies likely reflect differences in wind datasets, especially in western GoT, where geostrophic currents are relatively strong.

Ref. [7] reported a south-to-north intrusion into the GoT during the SWM based on a two-dimensional model, whereas our results indicate a strong outflow (Figure 9g). Other dissimilarities are observed at the southern GoT (7–8° N), where our model shows clockwise circulation, contrasting with their counterclockwise pattern during SWM and early INM2. Compared with the three-dimensional hydrodynamic model of [8], our results better capture the SWM outflow, though our results are not perfectly match with a clockwise-counterclockwise circulation in the central GoT or the strong southward flow from the UGoT during INM2. The identical clockwise circulation in the center of the GoT in our study is also less depicted in other three-dimensional hydrodynamic models [9,17]. These discrepancies in circulation may also be attributed to the computational grid resolution, where a finer grid provides more accurate results [19].

3.2.6. Exchange Flow Between the GoT and the SCS Variations

Cross-sectional flow velocity at the mouth of the GoT (Section 1, Figure 2) exhibits distinct seasonal variations. During the NEM, water predominantly flows out of the GoT along the western part of Section 1 near Kota Bharu, Malaysia, extending from the surface to near bottom, with maximum velocity near the surface. The depth of this outward flow decreases progressively along the section until 150 km from the shore. In contrast, strong inward flow is found at the eastern part of Section 1, with the velocity being strongest near the surface and gradually weakening with depth (Figure 10a). A similar pattern persists during the INM1, although the inflow velocity largely reduces, and the extent of the outward flow zone becomes more limited (Figure 10b).

During SWM, the cross-sectional flow displays characteristics of an estuarine circulation, where surface water (above ~20 m depth) flows outward from the GoT while bottom water from the SCS intrudes into the GoT (Figure 10c). This vertical structure of the current varies spatially along the section; specifically, in the region between 50 and 150 km and 200–250 km from the Kota Bharu coast, the outward flow is truncated below the 20 m depth. The INM2 displays a more complex distribution (Figure 10d). During this season, the outward flow divides into two separate zone (0–50 km and 150–200 km), separated by a localized inward flow, while a strong inward current is found near CMC.

The cross-sectional flow at the mouth of the GoT clearly indicate alternation of inflow and outflow between the GoT and the SCS, consistent with observations from the NAGA expedition reported by [3]. Ref. [5] showed surface outflow and subsurface inflow beginning in the INM1 (April) and continuing through the INM2 (November), driven primarily by density-induced circulation. This estuarine circulation was also observed during summer by [15], who further reported an inverse estuarine circulation at the mouth during winter. However, our results further indicate that the circulation patterns at the mouth are more complex than those described in previous studies.

The analysis of the GoT water-mass budget, with the considered domain delineated by the red-shaded area in Figure 2, reveals pronounced seasonal variability. A positive net budget is observed during the NEM (501 $m^3\ s^{-1}$) and INM2 (2450 $m^3\ s^{-1}$), indicating net inflow of water from the SCS into the GoT. In contrast, negative net budgets occur during INM1 (−17,391 $m^3\ s^{-1}$) and the SWM (−12,940 $m^3\ s^{-1}$), reflecting net outflow from the GoT.

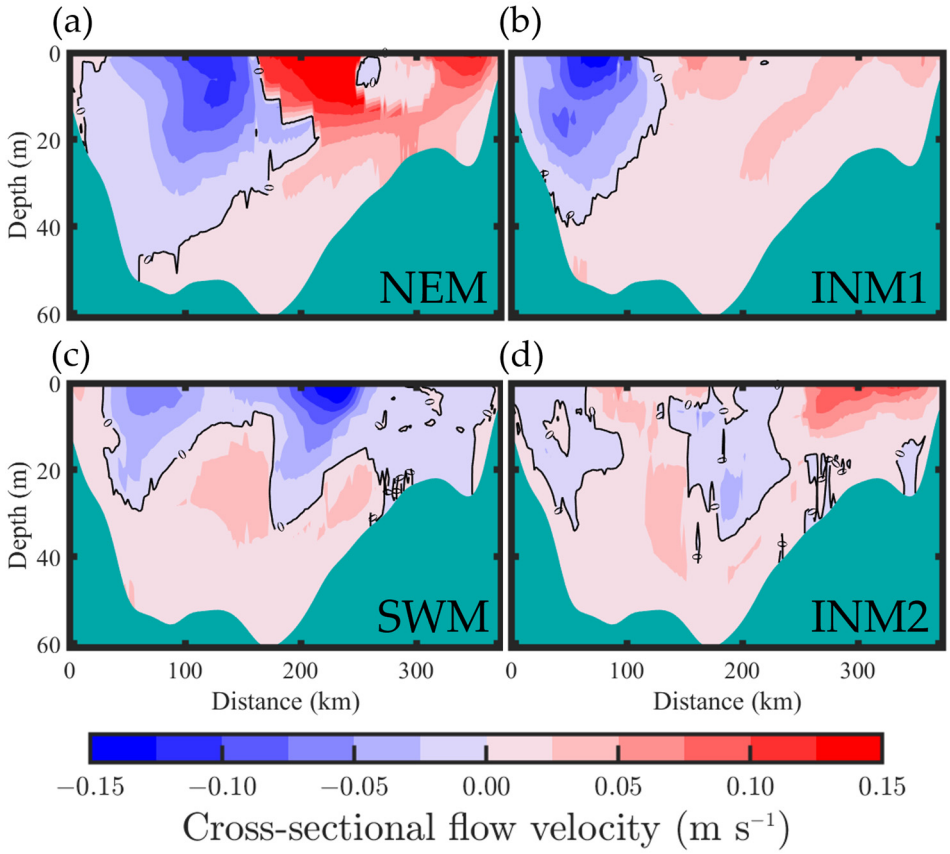

Figure 10. Cross-sectional flow velocity at Section 1 in each season: (**a**) NEM; (**b**) INM1; (**c**) SWM; (**d**) INM2. Red shading indicates flow into the GoT, while blue shading represents flow out of the GoT. The black line denotes the boundary separating inflow and outflow regions. The section extends from the Kota Bharu, Malaysia (0 km) to the CMC (373 km).

On an annual basis, Model C indicates that the GoT exhibits a negative net water budget, implying an overall export of approximately 218 km^3 of water from the GoT to the SCS. Freshwater input to the GoT is dominated by direct precipitation (708 km^3) and river discharge (48 km^3), whereas freshwater loss through evaporation amounts to −504 km^3. The remaining freshwater retained within the GoT is estimated to be approximately 34 km^3.

4. Conclusions

This study investigates the seasonal variability of hydrographic conditions in the GoT using a high-resolution hydrodynamic model reinforced by newly available datasets with enhanced spatial and temporal resolution. The results display complex variability in both surface and subsurface hydrographic properties, highlighting distinct dynamical features of the GoT circulation. A persistent seasonal anti-cyclonic gyre (clockwise gyre) is identified in the central part of GoT. This central gyre functions as a semi-enclosed structure that promotes trapping water, forming surface elevation, and inducing downwelling. In addition, a smaller secondary anticyclonic circulation is detected within the basin.

The study also provides new insights into volume transport in the GoT and its exchange with the adjacent SCS, which contributes to seasonal sea-level variability. Nevertheless, further analyses are required to identify the dominant physical drivers governing this variability. Future research will focus on elucidating the controlling mechanisms of GoT–SCS interactions, examining hydrographic and exchange variability at interannual timescales, and assessing the influence of large-scale atmospheric and oceanic climate

modes—such as the El Niño–Southern Oscillation (ENSO) and the Indian Ocean Dipole (IOD)—on the three-dimensional hydrography of the GoT.

Author Contributions: Conceptualization, K.P., T.P., A.A., A.B. and X.G.; methodology, K.P., T.P., A.A. and X.G.; validation, K.P. and T.P.; formal analysis, K.P.; investigation, K.P.; resources, T.P.; writing—original draft preparation, K.P.; writing—review and editing, K.P., T.P., A.A., A.B. and X.G.; visualization, K.P.; supervision, T.P.; funding acquisition, T.P. All authors have read and agreed to the published version of the manuscript.

Funding: This research was funded by the Thailand Research Fund (TRF) and the National Research Council of Thailand (NRCT), under the Ministry of Higher Education, Science, Research, and Innovation, which provided support through the Royal Golden Jubilee (RGJ) Ph.D. Programme, specifically under Grant No. PHD/0146/2561.

Data Availability Statement: Data associated with this article are not publicly available at this time due to the continuation of the study.

Acknowledgments: The authors would like to express their sincere appreciation to the Hydrographic Department of the Royal Thai Navy for providing valuable data, the Hydro-Informatics Institute (HII) for providing data from the GOT001 station, and the Marine observation and modeling database system for oceanography research in Thailand, and the Southeast Asian Fisheries Development Center (SEAFDEC) for the hydrographic observation data. Furthermore, this study would not have been possible without the equipment and laboratory facilities provided by Estuarine and Coastal Dynamics Modeling Laboratory, Department of Marine Science, Faculty of Fisheries, Kasetsart University.

Conflicts of Interest: The authors declare no conflicts of interest.

Abbreviations

The following abbreviations are used in this manuscript:

NEM	Northeast monsoon
CMC	Ca Mau Cape
INM2	Second inter monsoon
UGoT	Upper Gulf of Thailand
Model C	Climatological Model
Model E	Evaluation Model
GOFS	Global Ocean Forecasting System
R^2	Coefficient of determination
RMSE	Root mean square error
INM1	First inter monsoon
PVC	Polyvinyl chloride

Appendix A

Table A1. Data logger deployment details.

Stations	Latitude (°N)	Longitude (°E)	Depth (m)	Deployment Period
Ko Mannai	12.612863	101.686762	3	6 October 2019–4 April 2021
Sriracha (GOT001)	13.185862	100.916911	4.5	26 January 2018–1 January 2020
Ko Tao	10.08423	99.823578	3	2 March 2020–12 January 2021

Table A2. The details of the GOT model setup and forcing.

Setup Lists	Evaluation Model (Model E)	Climatological Model (Model C)
Simulation period	2015–2020	A three-year repeated simulation
Evaluation period	2016–2020	-
Warm-up period	2015	The first two years
Type of grid	Structured grid	
Grid cell size	~2.8 km × ~2.8 km	
Total number of grid cell	131,244	
Number of vertical layers	Ten layers in σ coordinate system	
Initial conditions	Water temperature and salinity from Global Ocean Forecasting System (GOFS) 3.1 on 1 January 2015	15-year climatological (2006–2020) water temperature and salinity data from the GOFS
Simulation time step	300 s	
Bottom roughness	Chézy coefficient at 70 $m^{1/2}$ s^{-1}	
Background horizontal eddy viscosity	10 m^2 s^{-1}	
Background horizontal eddy diffusivity	30 m^2 s^{-1}	
Background vertical eddy viscosity	1×10^{-6} m^2 s^{-1}	
Turbulence closure model	k-Epsilon	
Mean water density	1025 kg m^{-3}	
River discharge data	Global Flood Awareness System	
Offshore boundaries condition	Astronomical water elevation was derived from TPXO9 using 14 tidal components, along with the seasonal sea level changes in the SCS. The depth-varying vertical distributions of water temperature and salinity were derived from the GOFS.	
Meteorological forcing	ERA5 (3-h): northward and southward components of wind at a height of 10 m; temperature of air at 2 m height above surface; total precipitation; total cloud cover; mean sea level pressure; relative humidity	

Table A3. Overview of the Model E evaluation configuration.

Stations	Parameters	Data Interval	Evaluation Period (Day/Month/Year)
Laem Sing	Water level	Hourly	1 January 2016–31 December 2020
Ko Mannai	Water temperature	30 min	6 October 2019–31 December 2020
Sriracha (GOT001)	Water level	30 min	1 March 2018–31 December 2020
	Water temperature	30 min	1 March 2018–31 December 2020
	Salinity	30 min	1 March 2018–31 December 2020
	Eastward velocity (3 h filtered)	30 min	6 March 2020–31 December 2020
	Northward velocity (3 h filtered)	30 min	6 March 2020–31 December 2020
	Total magnitude (3 h filtered)	30 min	6 March 2020–31 December 2020

Table A3. *Cont.*

Stations	Parameters	Data Interval	Evaluation Period (Day/Month/Year)
Hua Hin	Water level	Hourly	1 January 2016–31 December 2020
Ko Lak	Water level	Hourly	1 January 2016–31 December 2020
Ko Mattaphon	Water level	Hourly	1 January 2016–31 December 2020
Ko Tao	Water level	30 min	2 March 2020–30 December 2020
	Water temperature	30 min	2 March 2020–30 December 2020
Ko Prap	Water level	Hourly	1 January 2016–31 December 2020
Geting	Water level	Monthly	January 2016–October 2017
Vung Tau	Water level	Hourly	1 January 2016–24 August 2020

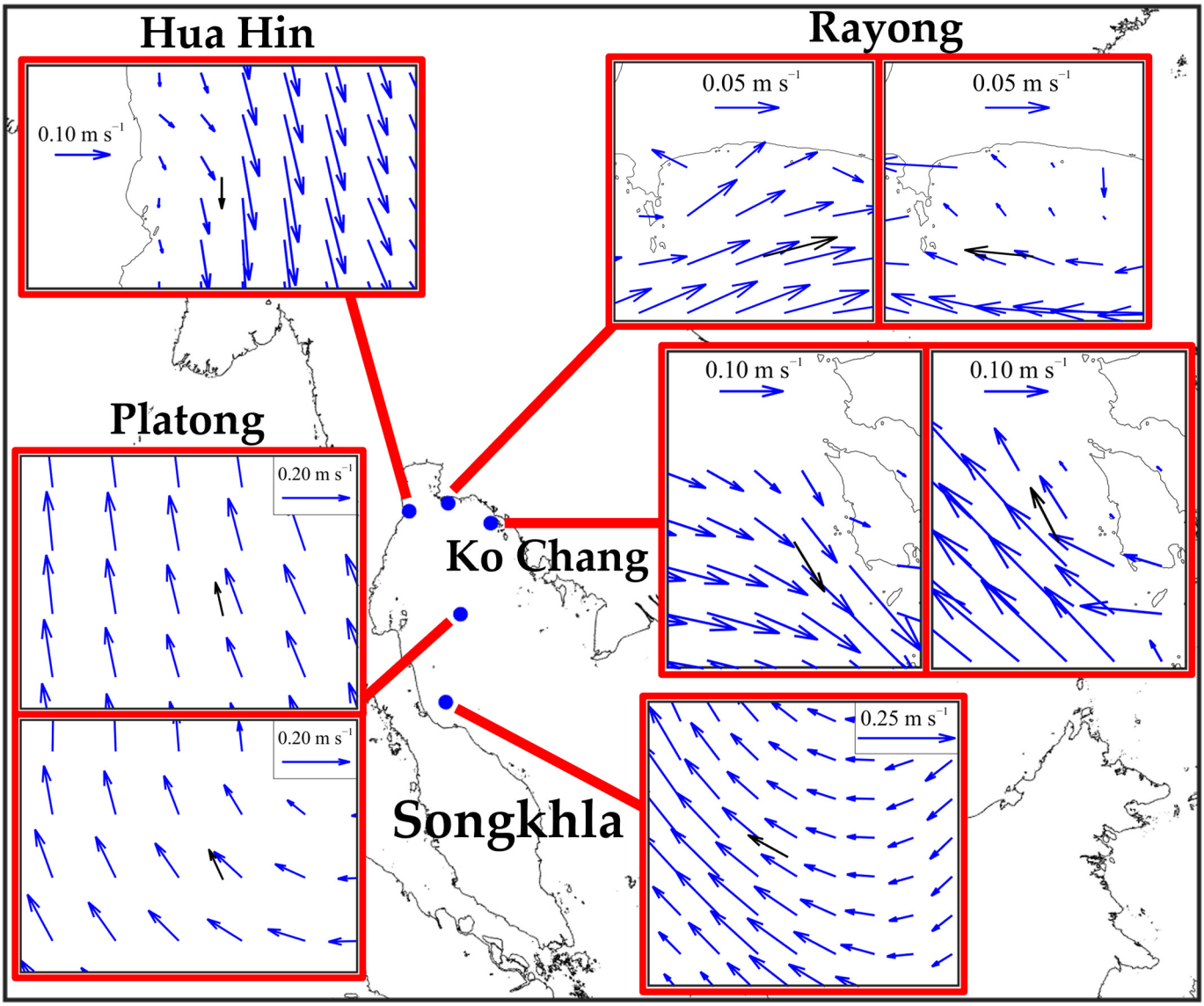

Figure A1. Monthly surface residual current vectors adapted and modified from [18]. Black arrows indicate the SEAWATCH buoy measurements, and blue arrows represent the Model C results across multiple locations and selected months: Hua Hin (September); Rayong (June–(**left**), November–(**right**)); Ko Chang (August–(**left**), November–(**right**)); Platong (January–(**top**), September–(**bottom**)); and Songkhla (April).

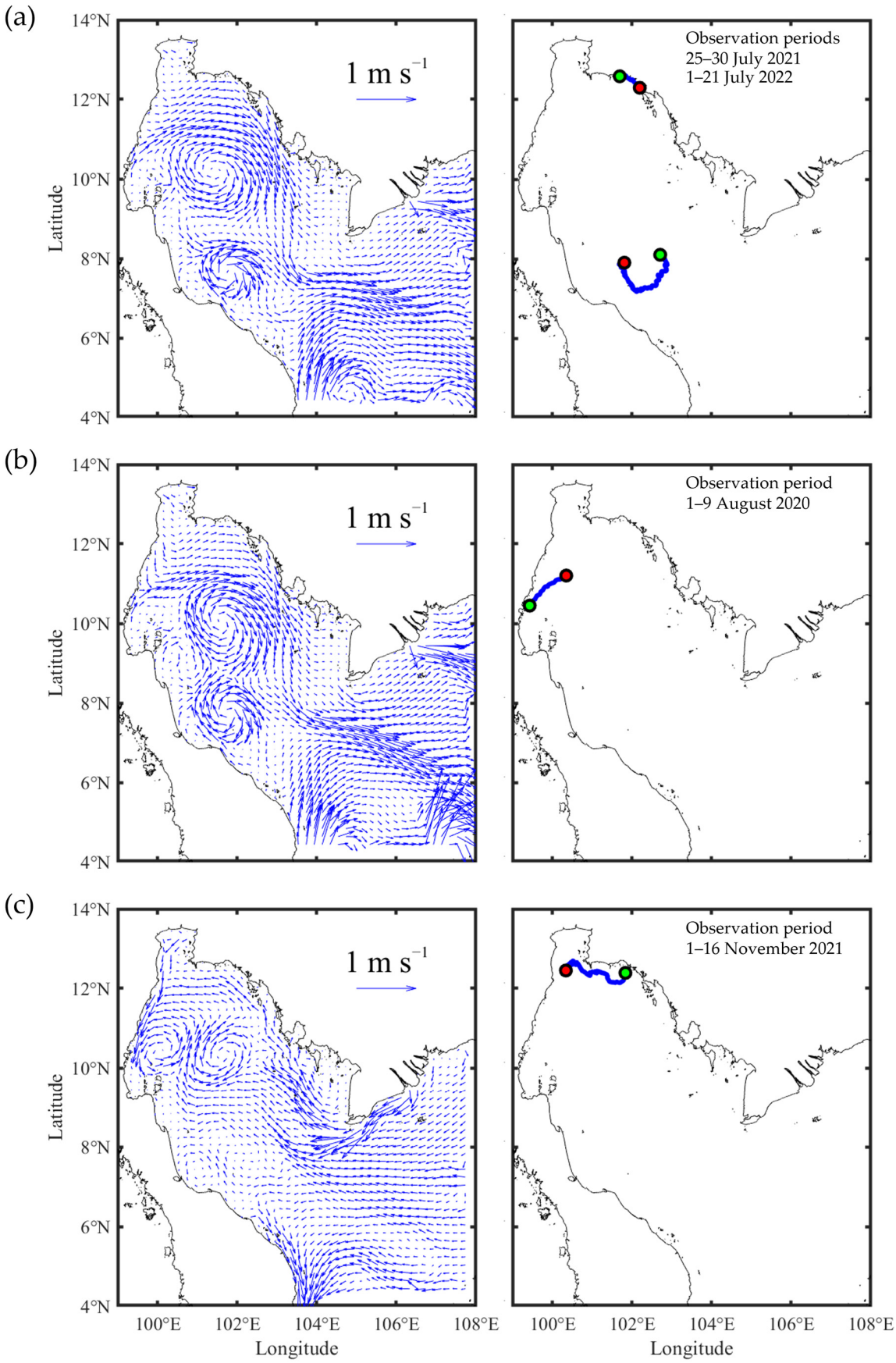

Figure A2. Comparison of simulated monthly surface residual currents from the Model C (**left**) against satellite-tracked buoy trajectories ((**right**); blue lines): (**a**) July; (**b**) August; (**c**) November. Green and red dots represent the release and end points of the buoy, respectively.

References

1. PEMSEA; Department of Marine and Coastal Resources (DMCR). *National State of Oceans and Coasts 2018: Blue Economy Growth of Thailand*; Partnerships in Environmental Management for the Seas of East Asia (PEMSEA): Quezon City, Philippines, 2019; p. 270.
2. Food and Agriculture Organization of the United Nations (FAO). Promoting the Blue Economy and Strengthening Fisheries Governance of the Gulf of Thailand Through the Ecosystem Approach to Fisheries (GoTFish Project). Available online: https://openknowledge.fao.org/server/api/core/bitstreams/1e6640ef-559d-4de1-bf64-b975acf8be3f/content (accessed on 25 May 2025).
3. Robinson, M.K. The Physical Oceanography of the Gulf of Thailand, Naga Expedition. Available online: https://escholarship.org/uc/item/4mf3d0b7 (accessed on 3 May 2025).
4. Stansfield, K.; Garrett, C. Implications of the salt and heat budgets of the Gulf of Thailand. *J. Mar. Res.* **1997**, *55*, 935–963. [CrossRef]
5. Buranapratheprat, A.; Luadnakrob, P.; Yanagi, T.; Morimoto, A.; Qiao, F. The modification of water column conditions in the Gulf of Thailand by the influences of the South China Sea and monsoonal winds. *Cont. Shelf Res.* **2016**, *118*, 100–110. [CrossRef]
6. Yanagi, T.; Takao, T.; Morimoto, A. Co-tidal and co-range charts in the South China Sea derived from satellite altimetry data. *La Mer* **1997**, *35*, 85–93.
7. Buranapratheprat, A.; Bunpapong, M. A Two-Dimensional Hydrodynamic Model for the Gulf of Thailand. In Proceedings of the IOC/WESTPAC Fourth International Scientific Symposium, Okinawa, Japan, 2–7 February 1998.
8. Yanagi, T.; Takao, T. Seasonal variation of three-dimensional circulations in the Gulf of Thailand. *La Mer* **1998**, *36*, 43–55.
9. Leenawarat, D. *The Investigation of the Residence Time of Water Mass in the Gulf of Thailand by Using a Hydrodynamic Model*; Burapha University: Chonburi, Thailand, 2018.
10. Snidvongs, A.; Sojisuporn, P. Numerical Simulations of The Net Current in the Gulf of Thailand Under Different Monsoon Regimes. In Proceedings of the First Technical Seminar on Marine Fishery Resources Survey in the South China Sea, Area I: Gulf of Thailand and Peninsular Malaysia, Bangkok, Thailand, 24–26 November 1997.
11. Sojisuporn, P.; Morimoto, A.; Yanagi, T. Seasonal variation of sea surface current in the Gulf of Thailand. *Coast. Mar. Sci.* **2010**, *34*, 91–102.
12. Li, J.; Zhang, R.; Ling, Z.; Bo, W.; Liu, Y. Effects of Cardamom Mountains on the formation of the winter warm pool in the gulf of Thailand. *Cont. Shelf Res.* **2014**, *91*, 211–219. [CrossRef]
13. Morimoto, A.; Mino, Y.; Buranapratheprat, A.; Kaneda, A.; Tong-U-Dom, S.; Sunthawanic, K.; Yu, X.; Guo, X. Hypoxia in the Upper Gulf of Thailand: Hydrographic observations and modeling. *J. Oceanogr.* **2021**, *77*, 859–877. [CrossRef]
14. Pokavanich, T.; Worrawatanathum, V.; Phattananuruch, K.; Koolkalya, S. Seasonal Dynamics and Three-Dimensional Hydrographic Features of the Eastern Gulf of Thailand: Insights from High-Resolution Modeling and Field Measurements. *Water* **2024**, *16*, 1962. [CrossRef]
15. Higuchi, M.; Anongponyoskun, M.; Phaksopa, J.; Onishi, H. Influence of monsoon-forced Ekman transport on sea surface height in the Gulf of Thailand. *Agric. Nat. Resour.* **2020**, *54*, 205–210. [CrossRef]
16. Anutaliya, A. Surface circulation in the Gulf of Thailand from remotely sensed observations: Seasonal and interannual timescales. *Ocean Sci.* **2023**, *19*, 335–350. [CrossRef]
17. Sripoonpan, P. *Characteristics and Mechanisms of Coastal Upwelling in the Gulf of Thailand*; Chulalongkorn University: Bangkok, Thailand, 2019.
18. Phattananuruch, K.; Pokavanich, T. Monsoon-Driven Dispersal of River-Sourced Floating Marine Debris in Tropical Semi-Enclosed Waters: A Case Study in the Gulf of Thailand. *J. Mar. Sci. Eng.* **2024**, *12*, 2258. [CrossRef]
19. Hewitt, H.T.; Bell, M.J.; Chassignet, E.P.; Czaja, A.; Ferreira, D.; Griffies, S.M.; Hyder, P.; McClean, J.L.; New, A.L.; Roberts, M.J. Will high-resolution global ocean models benefit coupled predictions on short-range to climate timescales? *Ocean Model.* **2017**, *120*, 120–136. [CrossRef]
20. Babagolimatikolaei, J. A comparative study of the sensitivity of an ocean model outputs to atmospheric forcing: ERA-Interim vs. ERA5 for Adriatic Sea Ocean modelling. *Dyn. Atmos. Ocean.* **2025**, *109*, 101525. [CrossRef]
21. Booncherm, C.; Vongpintu, V.; Nutpramoon, R. The characteristic of the sea surface residual flow and the circulation in the Gulf of Thailand from the long term collected data of the SEAWATCH Thailand program. In Proceedings of the 39th Kasetsartsart University Annual Conference, Bangkok, Thailand, 5–7 February 2001.
22. Deltares. *Delft3D-FLOW, User Manual*; Deltares: Delft, The Netherlands, 2018; p. 672.
23. Egbert, G.D.; Erofeeva, S.Y. Efficient Inverse Modeling of Barotropic Ocean Tides. *J. Atmos. Ocean. Technol.* **2002**, *19*, 183–204. [CrossRef]
24. Erofeeva, S.; Padman, L.; Howard, S. Tide Model Driver (TMD) Version 2.5, Toolbox for Matlab, 2020. Available online: https://github.com/EarthAndSpaceResearch/TMD_Matlab_Toolbox_v2.5 (accessed on 23 January 2026).
25. Amiruddin, A.M.; Haigh, I.D.; Tsimplis, M.N.; Calafat, F.M.; Dangendorf, S. The seasonal cycle and variability of sea level in the South China Sea. *J. Geophys. Res. Ocean.* **2015**, *120*, 5490–5513. [CrossRef]

26. Hersbach, H.; Bell, B.; Berrisford, P.; Hirahara, S.; Horányi, A.; Muñoz-Sabater, J.; Nicolas, J.; Peubey, C.; Radu, R.; Schepers, D.; et al. The ERA5 global reanalysis. *Q. J. R. Meteorol. Soc.* **2020**, *146*, 1999–2049. [CrossRef]
27. Harrigan, S.; Zsoter, E.; Alfieri, L.; Prudhomme, C.; Salamon, P.; Wetterhall, F.; Barnard, C.; Cloke, H.; Pappenberger, F. GloFAS-ERA5 operational global river discharge reanalysis 1979–present. *Earth Syst. Sci. Data* **2020**, *12*, 2043–2060. [CrossRef]
28. Zhong, W.; Lin, J.; Zou, Q.; Wen, Y.; Yang, W.; Yang, G. Hydrodynamic effects of large-scale suspended mussel farms: Field observations and numerical simulations. *Front. Mar. Sci.* **2022**, *9*, 973155–973172. [CrossRef]
29. Morimoto, A.; Yoshimoto, K.; Yanagi, T. Characteristics of Sea Surface Circulation and Eddy Field in the South China Sea Revealed by Satellite Altimetric Data. *J. Oceanogr.* **2000**, *56*, 331–344. [CrossRef]
30. Twigt, D.J.; De Goede, E.D.; Schrama, E.J.O.; Gerritsen, H. Analysis and modeling of the seasonal South China Sea temperature cycle using remote sensing. *Ocean Dyn.* **2007**, *57*, 467–484. [CrossRef]
31. Liu, Q.; Jiang, X.; Xie, S.-P.; Liu, W.T. A gap in the Indo-Pacific warm pool over the South China Sea in boreal winter: Seasonal development and interannual variability. *J. Geophys. Res. Ocean.* **2004**, *109*. [CrossRef]
32. Thompson, B.; Tkalich, P.; Malanotte-Rizzoli, P.; Fricot, B.; Mas, J. Dynamical and thermodynamical analysis of the South China Sea winter cold tongue. *Clim. Dyn.* **2016**, *47*, 1629–1646. [CrossRef]
33. Guo, J.; Qu, D.; Zhang, Z.; Sangmanee, C.; Chanthasiri, N.; Guo, B. Thermohaline conditions and circulation in the Gulf of Thailand during the northeast monsoon. *Cont. Shelf Res.* **2021**, *225*, 104487. [CrossRef]
34. Pinyoporn, W. *Seasonal Variation of Characteristic of Water Masses in the Gulf of Thailand and South China Sea*; Chulalongkorn University: Bangkok, Thailand, 1986.